How to cite: *Angew. Chem. Int. Ed.* **2023**, *62*, e202304010
doi.org/10.1002/anie.202304010

Polymers

Mucin-Inspired Single-Chain Polymer (MIP) Fibers as Potent SARS-CoV-2 Inhibitors

Raju Bej, Chuanxiong Nie, Kai Ludwig, Vahid Ahmadi, Jakob Trimpert, Julia M. Adler, Tatyana L. Povolotsky, Katharina Achazi, Marten Kagelmacher, Ricardo Martin Vidal, Jens Dernedde, Benedikt B. Kaufer, and Rainer Haag**

Abstract: Mucins are the key component of the defensive mucus barrier. They are extended fibers of very high molecular weight with diverse biological functions depending strongly on their specific structural parameters. Here, we present a mucin-inspired nanostructure, produced via a synthetic methodology to prepare methacrylate-based dendronized polysulfates (**MIP-1**) on a multi gram-scale with high molecular weight (MW = 450 kDa) and thiol end-functionalized mucin-inspired polymer (**MIP**) via RAFT polymerization. Cryo-electron tomography (Cryo-ET) analysis of **MIP-1** confirmed a mucin-mimetic wormlike single-chain fiber structure (length = 144 ± 59 nm) in aqueous solution. This biocompatible fiber showed promising activity against SARS-CoV-2 and its mutant strain, with a remarkable low half maximal (IC_{50}) inhibitory concentration (IC_{50} = 10.0 nM). Additionally, we investigate the impact of fiber length on SARS-CoV-2 inhibition by testing other functional polymers (**MIPs**) of varying fiber lengths.

Mucus is a biological dynamic hydrogel that, among its many functions in humans, protects underlying epithelial cells from infection by respiratory viruses upon inhalation.[1] Primarily responsible for this function are secreted mucins, the key component of native mucus.[2] Mucins are generally extremely high-molecular-weight gel-forming glycoproteins.[3] The glycosidic domain of mucin contains functional groups such as sugar-containing sulfates and sialic acid, which are responsible for its defensive properties against diverse pathogens,[4] whereas the cysteine-rich domain at each terminus helps to form extended disulfide-linked structures[5] (Scheme 1a). Inspired by the chemical composition and morphology of mucin, some polymer- and peptide-based mucin-mimetic materials have been developed[6] to structurally mimic native mucin and be used in various biological applications, such as antiviral and antibacterial agents and microarrays. Several studies have confirmed that backbone stiffness[6a] and steric strains[6b] in the adjacent groups are the key parameters in synthesizing mucin-like long-chain fiber structures. Moreover, the efficacy of synthetic mucins in various biological applications strongly depends on their mucin-mimetic structural parameters such as molecular weight,[6e] morphology[6b] and specific functional groups;[6f] these dependencies reflect the impact of mucin's properties on its optimal functioning.

Broad-spectrum antiviral activities[4b] exhibited by native mucins, together with the promising application of synthetic mucins,[7] inspired us to develop a mucin-mimetic polymeric platform mimicking the structure of native mucins that could serve, depending on the specific functionalization, as a novel antiviral material against various respiratory viruses.

Dendritic polyglycerol (dPG) has structural similarities to sugar-based polymeric scaffolds and has shown several advantages, including good hydrophilicity and biocompatibility as well as low non-specific binding to proteins.[8] These properties guided us to design protected oligoglycerol-functionalized methacrylate monomer (M1) for polymerization (Scheme 1b) with the anticipation of two key benefits: that post-functionalization to the protected hydroxyl groups would provide enough steric crowding in the polymer chain; and that this crowding and the rigidity of methacrylate backbone would enable the polymeric system to attain an elongated structure that could structurally mimic native mucins.

Recent studies have highlighted that native mucin has great inhibitory potential for the inhibition of SARS-CoV-2 infection.[9] Considering the current state of the pandemic caused by different variants of the respiratory virus SARS-CoV-2, as a first attempt we were interested in investigating

[*] Dr. R. Bej, Dr. C. Nie, Dr. K. Ludwig, Dr. V. Ahmadi, Dr. T. L. Povolotsky, Dr. K. Achazi, M. Kagelmacher, Prof. Dr. R. Haag
Institut für Chemie und Biochemie, Freie Universität Berlin
Takustraße 3, 14195 Berlin (Germany)
E-mail: rajubej@zedat.fu-berlin.de
haag@zedat.fu-berlin.de

Dr. J. Trimpert, J. M. Adler, R. M. Vidal, Dr. B. B. Kaufer
Institut für Virologie, Freie Universität Berlin
Robert-von-Ostertag-Straße 7–13, 14163 Berlin (Germany)

M. Kagelmacher, Dr. J. Dernedde
Institut für Laboratoriumsmedizin, Klinische Chemie und Pathobiochemie, Charité—Universitätsmedizin Berlin
Augustenburger Platz 1, 13353 Berlin (Germany)

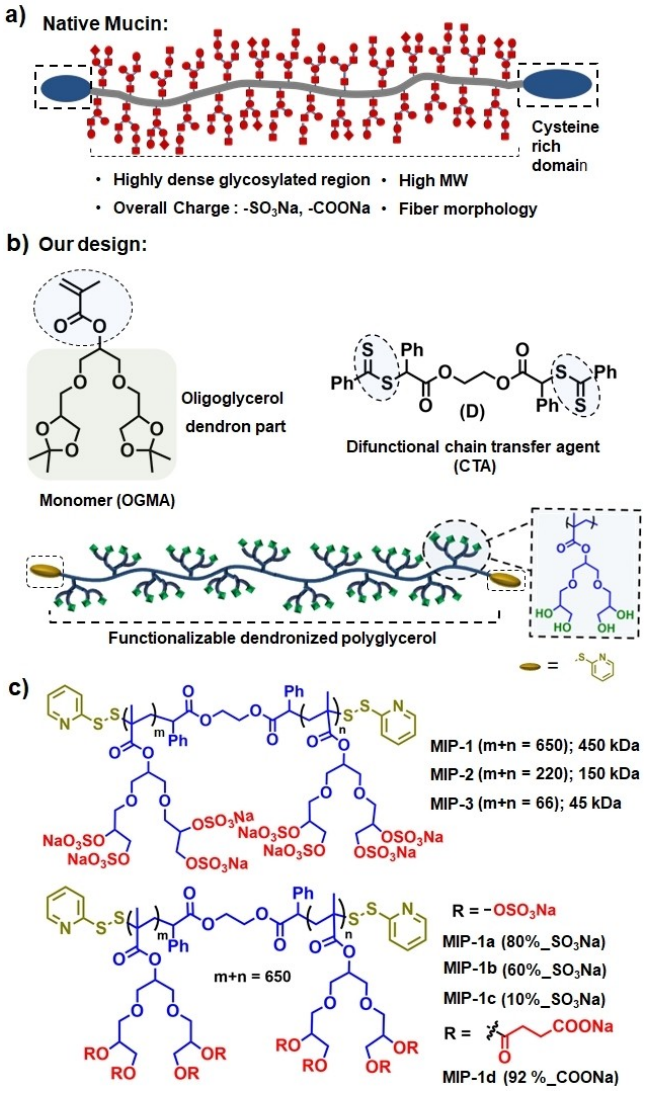

Scheme 1. a) Schematic representation of native mucin with selected characteristics; b) Schematic design of synthetic mucins together with chemical structure of monomer (M1) and chain transfer agent (CTA); c) Chemical structure of the mucin-inspired synthetic polymers (**MIPs**).

our synthetic platform to inhibit replication of this virus. The receptor-binding domain (RBD) of the SARS-CoV-2 spike protein is positively charged,[10] and so the negatively charged heparin has been developed as an antiviral for COVID-19 therapy.[11] Inspired by this work, our group has developed a series of promising sulfated inhibitors that can bind electrostatically to the SARS-CoV-2 spike protein and block the viral infection at its first step.[12] We therefore incorporated sulfate functional groups in our developed polymeric mucin-mimetic platform, expecting them to serve as potent inhibitors against SARS-CoV-2 due to their mucin-mimetic extended polymer chain properties.

Chemical structures of the developed synthetic polymers (**MIPs**) are shown in Scheme 1c. To synthesize them, we first optimized the polymerization conditions for monomer M1 (OGMA) using a difunctional chain transfer agent (CTA) to prepare different molecular weight polymers (POGMA) in gram-scale (Scheme S1).

The data on their characterization are detailed in the Supporting Information (Figure S1–S7 and Table S1). The terminal dithiocarbonate groups of POGMA were converted to 2-pyridyl disulfide (PDS) (Scheme S1), with UV/Vis analysis confirming the transformation (Figure S8). Quantification[13] of PDS groups indicated that they are located at both chain termini, confirming that polymerization had proceeded from both initiation sites. Subsequently, the acetonide groups were deprotected to generate hydroxyl functionalities (Figure S4–S6) and then the sulfate groups[14] were decorated to the side chain to obtain the final mucin-inspired polymers (**MIPs**: **MIP-1**, **MIP-2** and **MIP-3**). Their degree of sulfation was quantified by elemental analysis (Table S2); additional characterization data are presented in the Supporting Information (Figure S4–S6 and Figure S9). **MIP-1** was the longest-chain of the synthesize polymers, with a molecular weight of about 450 kDa falling within the same range as native mucin subunits.[3]

The expected overall strong negative charge of **MIPs** due to the sulfate groups was confirmed by negative zeta potential values (Table 1). To investigate the morphology of **MIP-1** in an aqueous solution, we employed cryo-electron microscopy (cryo-EM). Interestingly, we observed wormlike fibers (Figure 1a and Figure S10) that agree with our proposed structure. Since cryo-EM only provided projection images of the fibers spatially embedded in vitreous ice, we used cryo-electron tomography (cryo-ET) to determine their 3D structure and length (Figure 1c). A 3D volume calculated from a tilt series (-64 to $+64°$, increment 2°) is shown in Figure 1c (see also video S1 in the Supporting Information) and allows the determination of the actual length of the fibers. Tomogram analysis of 10 randomly selected fibers revealed a fiber length of 144 nm ($n=10$, SD = 59) and a width of $\approx$2 nm. This was consistent with the theoretical average length of $\approx$200 nm and average width of $\approx$2 nm of **MIP-1** (average repeat unit = 650) calculated based on the atomic distance in the polymer chain (Figure 1e). This

Table 1: Characterization and half maximal inhibitory concentration (IC_{50}) of polymers (**MIPs**) against B.1 variant of SARS-CoV-2 (in $\mu g\,mL^{-1}$ and in μM).

Polymers	MW[a]	DoF	ζ [mV]	IC_{50} [$\mu g\,mL^{-1}$]	IC_{50} [μM]
MIP-1	450	94	−63.1 ± 2.7	4.6 ± 1.4	0.01 ± 0.003
MIP-2	150	90	−51.3 ± 1.3	81.6 ± 21.2	0.54 ± 0.14
MIP-3	45	94	−35.7 ± 1.8	317.1 ± 102.9	7.04 ± 2.29
MIP-1a	412	80	−55.8 ± 0.9	7.1 ± 0.7	0.02 ± 0.002
MIP-1b	360	60	−42.7 ± 1.1	57.2 ± 24.1	0.16 ± 0.07
MIP-1c	227	10	−28.7 ± 3.6	2830.0 ± 1095.0	12.47 ± 4.8
MIP-1d	492	92	−47.2 ± 4.1	53.9 ± 17.0	0.11 ± 0.03
Heparin	13–15	NA	−38.2 ± 2.9	1400.0 ± 259.9	93.3 ± 17.3
BSM	NA	NA	−48.8 ± 2.6	443 ± 61.2	NA
POGMA-1b	200	0	−10.2 ± 1.7	4503 ± 431.1	22.5 ± 2.2

[a] ^{1}H NMR-determined molecular weight in kDa; DoF stands for degree of functionalization (either sulfates or carboxylate); Heparin, bovine submaxillary mucin (BSM) and non-sulfated MIP (POGMA-1b) were used as control.

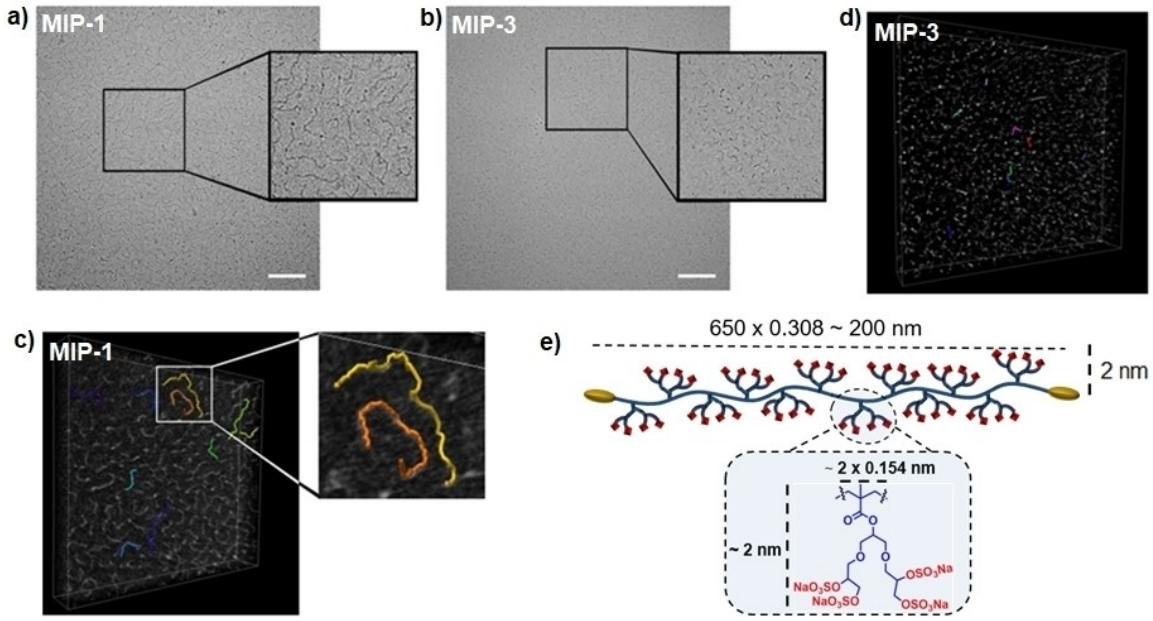

Figure 1. Cryo-electron micrograph of a) **MIP-1** and b) **MIP-3** in aqueous solution ($c = 1.0\ mg\,mL^{-1}$). Scale bar corresponds to 50 nm. A selected area of 100×100 nm (black box) is shown enlarged to reveal the ice-embedded polymer fibers more clearly; Sub-volume (approx. 500×450×70 nm) of a tomogram calculated from a tilt series of ice-embedded fibers from c) **MIP-1** as shown in (a) and d) **MIP-3** as shown in (b). Individual fibers were traced and measured with the interactive tracer-tool of the "Filament editor" of the Amira 3D software and are highlighted in different colors. e) Illustration of the theoretical dimensions of **MIP-1** on the basis of the schematic structure of the chain.

observation indicates that **MIP-1** forms single-chain fibers[15] in aqueous solution. The observed length distribution of fibers is plausible considering the polydispersity ($Đ = 1.5$) in **MIP-1**.

The fact that **MIP-1** forms single-chain fibers in aqueous solution suggests that the designed polymeric structural construct might be the key factor for extended single-chain fiber morphology. To confirm this, we examined the cryo-ET morphology of **MIP-3**, which is theoretically 10 times shorter than **MIP-1**. If our hypothesis of a single-chain fiber is correct, the shortest synthesized polymer **MIP-3** should also display single-chain fibers. Indeed, the aqueous solution of **MIP-3** (Figure 1b, Figure 1d and Figure S10) revealed fiber structures with a length of 25.7 nm ($n = 10$, SD = 10.3) closely matching the theoretical extended polymer chain length of ≈20 nm. Even more interestingly, due to the same repeating unit shared by polymers **MIP-1** and **MIP-3**, the fibers had a comparable width (≈2 nm), confirming the structural motif of a single-chain polymer fiber. Thus, we conclude that the methacrylate backbone, along with the electrostatic repulsion between the sulfated groups, imparts stiffness to the polymer chain, enhancing the polymers' ability to attain a mucin-like fiber structure.[5]

To evaluate the antiviral activity of the synthetic fibers, we tested them in a plaque reduction assay against the ancestral B.1 variant of SARS-CoV-2 (SARS-CoV-2/München-1.1/2020/929)[16] on Vero E6 cells (Figure 2). Cell morphology was recorded after pre-incubation of SARS-CoV-2 in the presence and absence of the synthesized fibers (Figure 2a–c). In the presence of **MIP-1**, most of the cells retain their morphology whereas in absence of **MIP-1** an increased cytopathic effect was observed indicating infection of the cells. The negligible number of infected cells in the presence of **MIP-1** confirmed its inhibitory activity against SARS-CoV-2 (Figure 2c). In parallel, as a control time dependent morphology of Vero E6 cells was recorded upto 72 h after incubation with only **MIP-1** (Figure 2d and Figure S11). To investigate the inhibition mechanism, we estimated binding constant (K_d) of **MIPs** with the spike protein (S1-His) of SARS-CoV-2 using microscale thermophoresis (MST) experiment (Figure 2e and Figure S12). Lower binding constant value for **MIPs** (Table S3) in comparison to the heparin control confirmed their strong binding to the spike proteins. Moreover, lower K_d value for **MIP-1** ($K_d = 740.22$ nM) (Figure 2e) in comparison to that of **MIP-3** ($K_d = 4.212$ μM) (Figure S12) indicate enhanced interaction for long chain fibers.

The analysis of dose-dependent virus inhibition curves (Figure 2f and Figure S13) indicated that the activity of the synthetic inhibitors depends on the molecular weight, and thus on the length of the polymer fibers (Table 1). The naturally occurring polysulfate heparin and native mucin, bovine submaxillary mucin (BSM) were used as controls (Figure S14). **MIP-1** showed a remarkably low half maximal inhibitory concentration in the nanomolar range ($c = 4.6 \pm 1.4\ \mu g\,mL^{-1}$, 10.0 ± 3.0 nM) (Table 1), making it the most efficient sulfated inhibitor reported to date for inhibiting SARS-CoV-2 infection by electrostatic interaction with the RBD of the spike protein and its activity is in the range (Table S4) of SARS-CoV-2 inhibition data of antibodies.[17] Moreover, IC_{50} values in Table 1 indicate that, while **MIP-1** is only 10 times longer than **MIP-3**, it is ≈70 times more

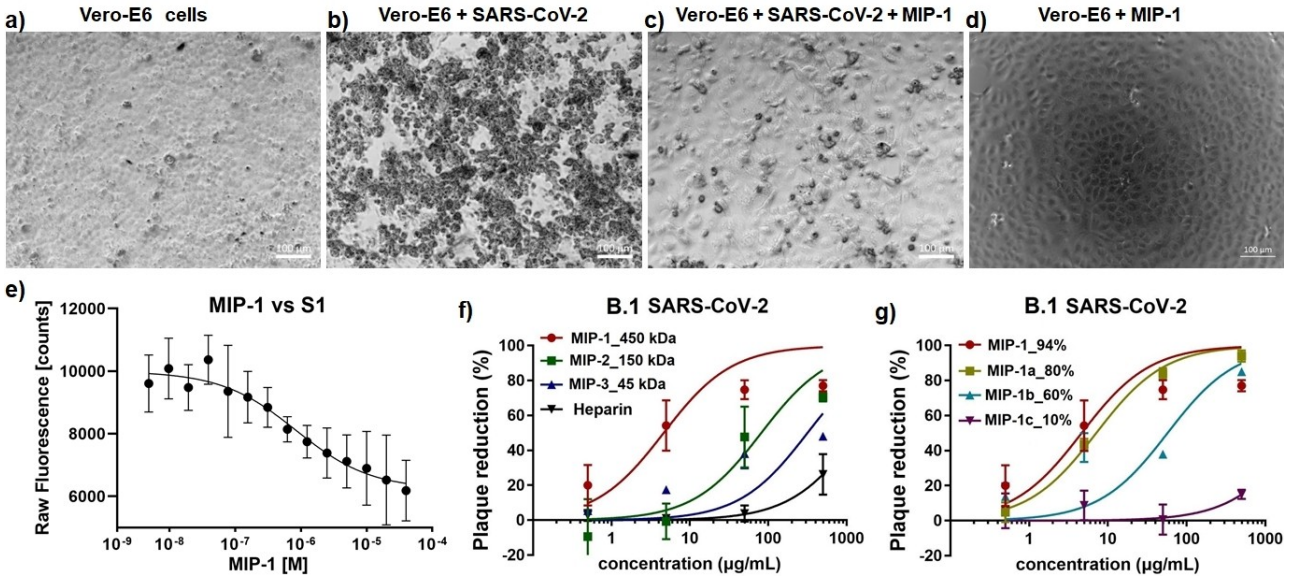

Figure 2. Inhibition of SARS-CoV-2 infection by **MIP-1**. Vero-E6 cells were incubated with virus solution in presence or absence of **MIP-1**. Representative bright-field microscopy images of a) Healthy Vero-E6 cells, b) Vero-E6 cells in absence of **MIP-1**, c) Vero-E6 cells in presence of **MIP-1** and d) Vero-E6 cells in presence of only **MIP-1** as a control. e) Microscale thermophoresis (MST) measurements of **MIP-1** against spike S1-His. Plaque reduction assay data estimating IC_{50} values for SARS-CoV-2 inhibition with B.1 variant: f) dose-dependent response for synthetic fibers (**MIP-1**, **MIP-2** and **MIP-3**) showing impact of fiber length on SARS-CoV-2 inhibition; Heparin was used as control. g) dose-dependent response for various degrees of sulfated derivatives of **MIP-1**, confirming impact of degree of sulfation on SARS-CoV-2 inhibition. In all cases values are expressed as mean ± SD, $n = 4$.

active against SARS-CoV-2. It thus appears that activity is, although depending on fiber length, not directly proportional to this parameter. This was further supported by our comparison of the inhibitory activity of **MIP-1** and **MIP-2**. Despite being only 3 times longer than **MIP-2**, **MIP-1** showed activity ≈18 times higher than that of **MIP-2**, emphasizing the influence of fiber length on inhibition. From this finding we hypothesize that the long-chain polymer fibers not only interact with the SARS-CoV-2 spike protein RBD via polyvalent interactions, but also provide steric shielding[18] that could prevent SARS-CoV-2 from binding to cell surface receptors (Scheme 2). In contrast, **MIP-2** and **MIP-3** interact less effectively due to their shorter fibers and cannot provide enough steric shielding to

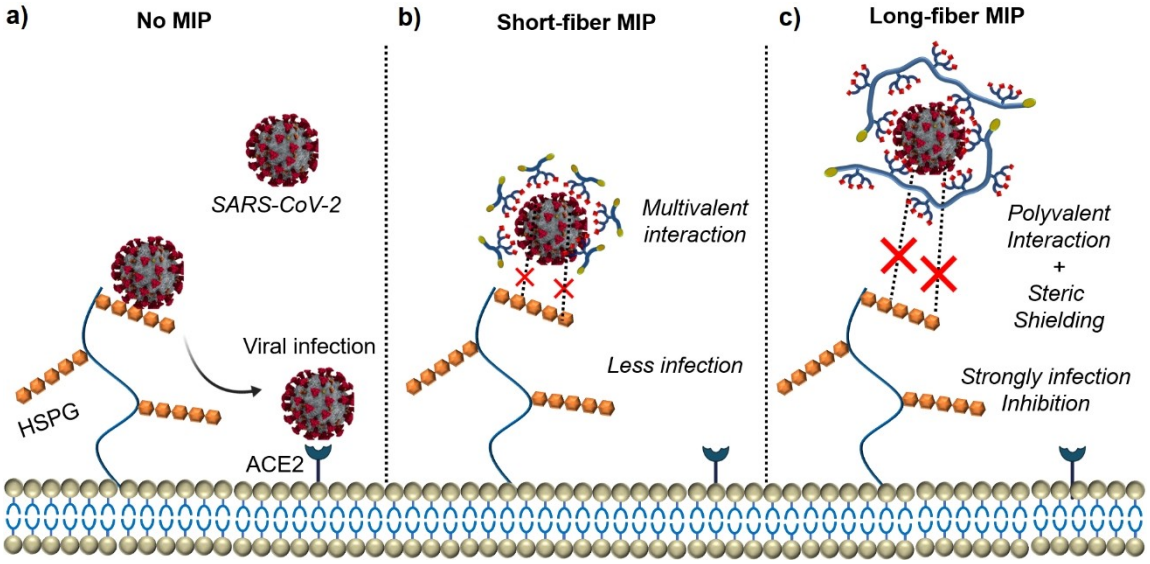

Scheme 2. a) SARS-CoV-2 enters host cells via interaction with cell surface proteins i.e Heparan Sulfate Proteoglycans (HSPG) and Angiotensin-Converting Enzyme 2 (ACE-2); Schematic illustration of a possible mechanism by which the mucin-inspired polymer (MIP) fibers could inhibit SARS-CoV-2 infection for b) short-fiber, **MIP-3** and c) long-fiber, **MIP-1**.

effectively prevent viral attachment to the cell surfaces. Thus, the combined effect of polyvalent interactions and steric shielding may be responsible for the remarkably low IC_{50} value ($c = 10.0$ nM) for SARS-CoV-2 inhibition by **MIP-1**. In order to see how long the materials can retain their protective properties, **MIP-1** was pre-incubated with cells for 24 h prior to SARS-CoV-2 infection and analyzed the infection (Figure S15) using fluorescence microscopy.[19] The significant reduction of infection in presence of **MIP-1** confirmed its preventive property even after 24 h of treatment.

To better understand the impact of the negative charge of the polymers on SARS-CoV-2 inhibition,[20] we synthesized several derivatives of **MIP-1**, the most potent inhibitor from our studies, by varying the degree of sulfation (**MIP-1a**, **MIP-1b** and **MIP-1c**); we then quantified the degree of sulfation of these derivatives by elemental analysis (Table 1 and Table S2). We found that ≈10 % sulfated polymer (**MIP-1c**) showed negligible SARS-CoV-2 inhibitory activity (Figure 2g) ($IC_{50} = 2830 \pm 1095\ \mu g\,mL^{-1}$). With increasing sulfation level, the zeta potential became more negative (Table 1), resulting in an increase in SARS-CoV-2 inhibitory activity (Figure 2g, Figure S14 and S15). This further confirms that electrostatic interaction with the RBD of the spike protein is responsible for the inhibition of SARS-CoV-2. In the light of the ongoing evolution of SARS-CoV-2, we further tested the potential of **MIP-1** to inhibit the SARS-CoV-2 Delta variant (Figure S16). Our results confirm excellent inhibitory activity ($IC_{50} \approx 4.2 \pm 2.0\ \mu g\,mL^{-1}$, 9.3 ± 4.4 nM) against this variant, suggesting that **MIP-1** has great potential to inhibit SARS-CoV-2 variants due to its charge-dependent and thus rather non-specific binding of the RBD.

Since it is known that the overall electronegative charge[21] of native mucins arises from functional sulfate as well as carboxylate groups, we synthesized (**MIP-1d**) carboxylate analogue of the most active polymer **MIP-1** (Scheme S2 and Figure S17). The plaque reduction assay of **MIP-1d** showed good inhibition with an IC_{50} about $53.9\ \mu g\,mL^{-1}$ (Figure S18) confirming that the carboxylate functional groups are also active in SARS-CoV-2 inhibition. Nevertheless, for our synthesized platform, the sulfated version of **MIP-1** proved to be more active than the carboxylate version.

The synthesized **MIPs** showed negligible cytotoxicity in various cell lines (Vero-E6, 16HBE14o, A549) (Figure S19–S22) upto 72 h of incubation. The inherent anticoagulant activity of sulfated polymers in general limits their direct applications. In this regard, **MIPs** showed negligible anticoagulant activity in comparison to heparin (Figure S23). Our studies indicated that the anticoagulant activity increased with decreasing polymer chain length[22] and with increasing degree of sulfation (Figure S24) but are significantly lower than that of heparin. We have also investigated anti-complement effect of **MIPs** (Figure S25). The complement inhibition study clearly demonstrates the sulfate dependent[23] anti-complement activity of the **MIPs**. Here, we observe a size dependent inhibition, **MIP-1** showed IC_{50} of 6.0 ± 0.3 nM whereas **MIP-3** gave an IC_{50} of 72.7 ± 8.1 nM.

In summary, we have developed a methodology for the gram-scale synthesis of methacrylate-based functionalized dendronized polyglycerols as novel mucin-mimetic polymers that form a wormlike single-chain fiber morphology. Apart from their high biocompatibility, low anticoagulant activity and complement inhibition activity, they exhibit great inhibitory potential against SARS-CoV-2 and its mutant strains. We found that mucin-mimetic properties such as molecular weight, morphology, length of fibers and functional groups (–SO_3Na, –COONa) are key parameters for the synthesized fibers' inhibitory activity against SARS-CoV-2. Our findings reflect the advantages of long-chain mucin-like fibers for the defensive properties of native mucus, and should guide the design of potent inhibitors. Considering the potential application of native mucins as lubricants,[24] antibacterial and antiviral coatings against broad-spectrum pathogens,[25] muco-adhesive materials[26] and mucosal drug vehicles,[27] these synthetic mucin-inspired polymers (**MIPs**) represent promising biomaterials for mucus related research and can potentially be used as active component in nasal spray against SARS-CoV-2.

Acknowledgements

R.B. thanks Alexander von Humboldt (AvH) Foundation for Postdoctoral Research Fellowship. R.B. and R.H. thank the Collaborative Research Center CRC1449, Project ID 431232613 and the German Science Foundation (DFG) for financial support. The authors would like to acknowledge the assistance of the Core Facility BioSupraMol supported by the DFG. We would like to thank Ms. Elisa Quaas and Dr. Stefanie Wedepohl for performing anticoagulant assays. We thank the European Virus Archive, D. Niemeyer and C. Drosten from Charité and D. Bourquain from the Robert-Koch-Institut for providing SARS-CoV-2 variants used in this study. VeroE6-TMPRSS cells were provided by the NIBSC Research Reagent Repository, UK, with thanks to Dr. Makoto Takeda. We are grateful to Benjamin Allen for his careful language editing. We thank the lab of Prof. Daniel Lauster for access to the picoMST device, which was funded by the Federal Ministry of Education and Science (BMBF; grant number: 13XP5111). Open Access funding enabled and organized by Projekt DEAL.

Conflict of Interest

The authors declare no conflict of interest.

Data Availability Statement

The data that support the findings of this study are available in the Supporting Information of this article.

Keywords: Biocompatibility · Mucin-Inspired Polymer · RAFT Polymerization · SARS-Cov-2 Inhibition · Single-Chain Fiber

[1] a) M. Zanin, P. Baviskar, R. Webster, R. Webby, *Cell Host Microbe* **2016**, *19*, 159–168; b) C. Werlang, G. Cárcarmo-Oyarce, K. Ribbeck, *Nat. Rev. Mater.* **2019**, *4*, 134–145.

[2] C. Ridley, D. J. Thornton, *Biochem. Soc. Trans.* **2018**, *46*, 1099–1106.

[3] a) D. J. Thornton, J. K. Sheehan, *Proc. Am. Thorac. Soc.* **2004**, *1*, 54–61; b) S. P. Authimoolam, T. D. Dziubla, *Polymer* **2016**, *8*, 71.

[4] a) K. M. Wheeler, G. Cárcamo-Oyarce, B. S. Turner, S. Dellos-Nolan, J. Y. Co, S. Lehoux, R. D. Cummings, D. J. Wozniak, K. Ribbeck, *Nat. Microbiol.* **2019**, *4*, 2146–2154; b) M. Chatterjee, J. P. M. van Putten, K. Strijbis, *mBio* **2020**, *11*, e02374-20.

[5] G. Javitt, L. Khmelnitsky, L. Albert, L. S. Bigman, N. Elad, D. Morgenstern, T. Ilani, Y. Levy, R. Diskin, D. Fass, *Cell* **2020**, *183*, 717–729.

[6] a) D. Rabuka, R. Parthasarathy, G. S. Lee, X. Chen, J. T. Groves, C. R. Bertozzi, *J. Am. Chem. Soc.* **2007**, *129*, 5462–5471; b) A. G. Kruger, S. D. Brucks, T. Yan, G. Cárcarmo-Oyarce, Y. Wei, D. H. Wen, D. R. Carvalho, M. J. A. Hore, K. Ribbeck, R. R. Schrock, L. L. Kiessling, *ACS Cent. Sci.* **2021**, *7*, 624–630; c) C.-S. Kwan, A. R. Cerullo, A. B. Braunschweig, *ChemPlusChem* **2020**, *85*, 2704–2721; d) J. R. Kramer, B. Onoa, C. Bustamante, C. R. Bertozzi, *Proc. Natl. Acad. Sci. USA* **2015**, *112*, 12574–12579; e) M. Wallert, C. Nie, P. Anilkumar, S. Abbina, S. Bhatia, K. Ludwig, J. N. Kizhakkedathu, R. Haag, S. Block, *Small* **2020**, *16*, 2004635; f) M. Cohen, H. P. Senaati, C. J. Fisher, M. L. Huang, P. Gagneux, K. Godula, *ACS Cent. Sci.* **2016**, *2*, 710–714.

[7] R. Bej, R. Haag, *J. Am. Chem. Soc.* **2022**, *144*, 20137–20152.

[8] M. Calderón, M. A. Quadir, S. K. Sharma, R. Haag, *Adv. Mater.* **2010**, *22*, 190–218.

[9] a) C. L. Wardzala, A. M. Wood, D. M. Belnap, J. R. Kramer, *ACS Cent. Sci.* **2022**, *8*, 351–360; b) M. Chatterjee, L. Z. X. Huang, C. Wang, A. Z. Mykytyn, B. Westendorp, R. W. Wubbolts, B.-J. Bosch, B. L. Haagmans, J. P. M. van Putten, K. Strijbis, *bioRxiv* **2021**, https://doi.org/10.1101/2021.10.29.466408.

[10] T. M. Clausen, D. R. Sandoval, C. B. Spliid, J. Pihl, H. R. Perrett, C. D. Painter, A. Narayanan, S. A. Majowicz, E. M. Kwong, R. N. McVicar, B. E. Thacker, C. A. Glass, Z. Yang, J. L. Torres, G. J. Golden, P. L. Bartels, R. N. Porell, A. F. Garretson, L. Laubach, J. Feldman, X. Yin, Y. Pu, B. M. Hauser, T. M. Caradonna, B. P. Kellman, C. Martino, P. L. S. M. Gordts, S. K. Chanda, A. G. Schmidt, K. Godula, S. L. Leibel, J. Jose, K. D. Corbett, A. B. Ward, A. F. Carlin, J. D. Esko, *Cell* **2020**, *183*, 1043–1057.

[11] R. Tandon, J. S. Sharp, F. Zhang, V. H. Pomin, N. M. Ashpole, D. Mitra, M. G. McCandless, W. Jin, H. Liu, P. Sharma, R. J. Linhardt, *J. Virol.* **2021**, *95*, e01987-20.

[12] a) C. Nie, P. Pouyan, D. Lauster, J. Trimpert, Y. Kerkhoff, G. P. Szekeres, M. Wallert, S. Block, A. K. Sahoo, J. Dernedde, K. Pagel, B. B. Kaufer, R. R. Netz, M. Ballauff, R. Haag, *Angew. Chem. Int. Ed.* **2021**, *60*, 15870–15878; b) I. S. Donskyi, C. Nie, K. Ludwig, J. Trimpert, R. Ahmed, E. Quaas, K. Achazi, J. Radnik, M. Adeli, R. Haag, K. Osterrieder, *Small* **2021**, *17*, 2007091; c) E. Mohammadifar, V. Ahmadi, M. Fardin Gholami, A. Oehrl, O. Kolyvushko, C. Nie, I. S. Donskyi, S. Herziger, J. Radnik, K. Ludwig, C. Böttcher, J. P. Rabe, K. Osterrieder, W. Azab, R. Haag, M. Adeli, *Adv. Funct. Mater.* **2021**, *31*, 2009003.

[13] a) R. Bej, P. Rajdev, R. Barman, S. Ghosh, *Polym. Chem.* **2020**, *11*, 990–1000; b) R. Bej, S. Ghosh in *Sulfur-Containing Polymers: From Synthesis to Functional Materials* (Eds.: X.-H. Zhang, P. Theato), Wiley-VCH, Weinheim, **2020**, pp. 367–389.

[14] F. Paulus, D. Steinhilber, P. Welker, D. Mangoldt, K. Licha, H. Depner, S. Sigrist, R. Haag, *Polym. Chem.* **2014**, *5*, 5020–5028.

[15] Y. Yamauchi, N. N. Horimoto, K. Yamada, Y. Matsushita, M. Takeuchi, Y. Ishida, *Angew. Chem. Int. Ed.* **2021**, *60*, 1528–1534.

[16] R. Wölfel, V. M. Corman, W. Guggemos, M. Seilmaier, S. Zange, M. A. Müller, D. Niemeyer, T. C. Jones, P. Vollmar, C. Rothe, M. Hoelscher, T. Bleicker, S. Brünink, J. Schneider, R. Ehmann, K. Zwirglmaier, C. Drosten, C. Wendtner, *Nature* **2020**, *581*, 465–469.

[17] a) C. Wang, W. Li, D. Drabek, N. M. A. Okba, R. v. Haperen, A. D. M. E. Osterhaus, F. J. M. van Kuppeveld, B. L. Haagmans, F. Grosveld, B.-J. Bosch, *Nat. Commun.* **2020**, *11*, 2251; b) Z. Ku, X. Xie, P. R. Hinton, X. Liu, X. Ye, A. E. Muruato, D. C. Ng, S. Biswas, J. Zou, Y. Liu, D. Pandya, V. D. Menachery, S. Rahman, Y.-A. Cao, H. Deng, W. Xiong, K. B. Carlin, J. Liu, H. Su, E. J. Haanes, B. A. Keyt, N. Zhang, S. F. Carroll, P.-Y. Shi, Z. An, *Nature* **2021**, *595*, 718–723.

[18] J. Vonnemann, S. Liese, C. Kuehne, K. Ludwig, J. Dernedde, C. Böttcher, R. R. Netz, R. Haag, *J. Am. Chem. Soc.* **2015**, *137*, 2572–2579.

[19] a) Y. Ma, G. Mao, G. Wu, M. Chen, F. Qin, L. Zheng, X.-E. Zhang, *ACS Appl. Mater. Interfaces* **2021**, *13*, 24477–24486; b) Y. Cheng, A. E. Clark, J. Zhou, T. He, Y. Li, R. M. Borum, M. N. Creyer, M. Xu, Z. Jin, J. Zhou, W. Yim, Z. Wu, P. Fajtová, A. J. O'Donoghue, A. F. Carlin, J. V. Jokerst, *ACS Nano* **2022**, *16*, 12305–12317.

[20] C. Nie, A. K. Sahoo, R. R. Netz, A. Hermann, M. Ballauff, R. Haag, *ChemBioChem* **2022**, *23*, e2021006.

[21] J. Leal, H. D. C. Smyth, D. Ghosh, *Int. J. Pharm.* **2017**, *532*, 555–572.

[22] D. Brooks, J. Kizhakkedathu, R. Shenoi, M. Weinhart, B. Lai, R. Haag, D. Groeger, US Patent-10392474, **2019**.

[23] K. Silberreis, N. Niesler, N. Rades, R. Haag, J. Dernedde, *Biomacromolecules* **2019**, *20*, 3809–3818.

[24] T. Crouzier, K. Boettcher, A. R. Geonnotti, N. L. Kavanaugh, J. B. Hirsch, K. Ribbeck, O. Lieleg, *Adv. Mater. Interfaces* **2015**, *2*, 1500308.

[25] G. Petrou, T. Crouzier, *Biomater. Sci.* **2018**, *6*, 2282–2297.

[26] M. T. Cook, S. L. Smith, V. V. Khutoryanskiy, *Chem. Commun.* **2015**, *51*, 14447–14450.

[27] M. Marczynski, C. Kimna, O. Lieleg, *Adv. Drug Delivery Rev.* **2021**, *178*, 113845.

Manuscript received: March 20, 2023
Accepted manuscript online: May 2, 2023
Version of record online: June 14, 2023